Mon. Not. R. Astron. Soc. **000**, 1–8 (2015) Printed 2 June 2015 (MN LATEX style file v2.2)

Pulsar Lensing Geometry

Siqi Liu[1,3]⋆, Ue-Li Pen[1,2]†, J-P Macquart[4]‡, Walter Brisken[5]§, Adam Deller[6]¶

[1] *Canadian Institute for Theoretical Astrophysics, University of Toronto, M5S 3H8 Ontario, Canada*
[2] *Canadian Institute for Advanced Research, Program in Cosmology and Gravitation*
[3] *Department of Astronomy and Astrophysics, University of Toronto, M5S 3H4, Ontario, Canada*
[4] *ICRAR-Curtin University of Technology, Department of Imaging and Applied Physics, GPO Box U1978, Perth, Western Australia 6102, USA*
[5] *National Radio Astronomy Observatory, P.O. Box O, Socorro, NM 87801, USA*
[6] *ASTRON, the Netherlands Institute for Radio Astronomy, Postbus 2, 7990 AA, Dwingeloo, The Netherlands*

2 June 2015

ABSTRACT

By analysing archival VLBI data of PSR B0834+06, we conclude that for this example the plasma lenses can be precisely modelled using the inclined sheet model (Pen & Levin 2014), resulting in two distinct lens planes. This data strongly favours the grazing sheet model over turbulence as the primary source of pulsar scattering. 7 observed apex parameters fit the model to percent accuracy. Comparison with VLBI proper motion results in a direct measure of the ionized ISM screen. The results are consistent with motions expected in the local galaxy. The simple 1-D structure of the lenses opens up the possibility of using interstellar lenses as precision probes for pulsar lens mapping, and new opportunities for removing scattering to improve pulsar timing. We describe the parameters and observables of this double screen system. While relative screen distances can in principle be accurately determined, a global conformal distance degeneracy exists which allows a rescaling of the absolute distance scale. This degeneracy is broken if the pulsar resides in a binary system, which is the case for most precision timing targets.

Key words: Pulsar

1 INTRODUCTION

Pulsars have long provided a rich source of astrophysical information due to their compact emission and predictable timing. One of the weakest measurements for most pulsars is their direct geometric distance. For some pulsars, timing parallax or VLBI parallax has resulted in direct distance determination. For most pulsars, the distance is a major uncertainty for precision timing interpretations, including mass, moment of inertia (Kramer et al. 2006; Lorimer & Kramer 2012), and gravitational wave direction (Boyle & Pen 2012).

Direct VLBI observation of PSR B0834+06 shows multiple images lensed by the interstellar plasma. Combining the angular positions and scintillation delays, the authors published the derived effective distance (Brisken et al. 2010) of approximately 1168±23 pc for apexes on the main scattering axis. This represents a precise measurement compared to all other attempts to derive distances to this pulsar. This effective distance is a combination of pulsar-screen and earth-screen distances, and does not allow a separate determination of the individual distances. A binary pulsar system would in principle allow a breaking of this degeneracy (Pen & Levin 2014). One potential limitation is the precision to which the lensing model can be understood. In this paper, we demonstrate that the lensing screen consists of nearly parallel linear refractive structures, in two screens. The precise model confirms the one dimensional nature, and thus the small number of parameters that quantify the lensing screen.

2 VLBI ASTROMETRY

PSR B0834+06 was observed 8 times with the Very Long Baseline Array (VLBA) between 2009 May and 2011 January. Four 16 MHz bands spread across the frequency range 1406 – 1692 MHz were sampled with 2 bit quantization in both circular polarizations, giving a total data rate of 512 Mbps per antenna. The primary phase calibrator was J0831+0429, which is separated from the target by 2.1 degrees, but the target field also included an in-beam calibra-

⋆ E-mail: sqliu@cita.utoronto.ca
† E-mail: pen@cita.utoronto.ca
‡ E-mail:J.Macquart@curtin.edu.au
§ Email:wbrisken@aoc.nrao.edu
¶ E-mail:deller@astron.nl

Table 1. Fitted and derived astrometric parameters for PSR B0834+06.

Reference right ascension (J2000)[a]	08:37:5.644606(9)
Reference declination (J2000)[a]	06:10:15.4047(1)
Position epoch (MJD)	55200
$\mu_{\mathrm{R.A.}}$ (mas yr^{-1})	2.16(19)
μ_{Dec} (mas yr^{-1})	51.64(13)
Parallax (mas)	1.63(15)
Distance (pc)	620(60)
v_{T} (km s^{-1})	150(15)

[a]The errors quoted here are from the astrometric fit only and do not include the ∼1 mas position uncertainty transferred from the in–beam calibrator's absolute position.

tor source J083646.4+061108, which is separated from PSR B0834+06 by only 5′. The cycle time between primary phase calibrator and target field was 5 minutes, and the total duration of each observation was 4 hours.

Standard astrometric data reduction techniques were applied (e.g., Deller et al. 2012, 2013), using a phase calibration solution interval of 4 minutes for the in-beam calibrator source J083646.4+061108. J083646.4+061108 is weak (flux density ∼4 mJy) and its brightness varied on the level of tens of percent. The faintness leads to noisy solutions, and the variability indicates that source structure evolution (which would be translate to offsets in the fitted target position) could be present. Together, these two effects lead to reduce astrometric precision compared to that usually obtained with VLBI astrometry using in-beam calibration, and the results presented here could be improved upon if the observations were repeated using the wider bandwidths and higher sensitivity now available with the VLBA, potentially in conjunction with additional in-beam background sources.

While a straightforward fit to the astrometric observables yields a pulsar distance with a formal error <1%, the reduced χ^2 of this fit is ∼40, indicating that the formal position errors greatly underestimate the true position errors, and that systematic effects such as the calibrator effects discussed above as well as residual ionospheric errors dominate. Accordingly, the astrometric parameters and their errors were instead obtained by bootstrap sampling (Efron & Tibshirani 1991). These results are presented in Table 1.

3 LENSING

In this section we map the data onto the grazing incidence sheet model. The folded sheet model is qualitatively analogous to the reflection of a street lamp across a lake as seen from the opposite shore. In the absence of waves, exactly one image forms at the point where the angle of incidence is equal to the angle of reflection. In the presence of waves, one generically sees a line of images above and below the unperturbed image. The grazing angle geometry simplifies the lensing geometry, effectively reducing it from a two dimensional problem to one dimension. The statistics of such reflections is sometimes called glitter, and has many solvable properties (Longuet-Higgins 1960). A similar effect occurs when the observer is below the surface. Two major distinctions arise: 1. the waves can deform the surface to create caustics in projection. Near caustics, Snell's law can lead to highly amplified refraction angles. 2. due to the odd image theorem, each caustic leads to two images. In practice, the surface could be caused be reconnection sheets (Braithwaite 2015), which have finite widths to regularize these singularities. Diffusive structures have Gaussian profiles, which was analysed in Pen & King (2012). The lensing details differ for convergent (underdense) *vs* divergent (overdense) lenses, first considered by Clegg et al. (1998).

The generic interstellar electron density is insufficient to deflect radio waves by the observed ∼ mas bending angles. At grazing incidence, Snell's law results in an enhanced bending angle, which formally diverges. Magnetic discontinuities generically propagate as transverse surface waves, whose restoring force is the change in Alfvén speed on the two sides of the discontinuity. This completes the analogy to waves on a lake: for sufficiently inclined sheets the waves will appear to fold back onto themselves in projection on the sky. At each fold caustic, Snell's law diverges, leading to enhanced refractive lensing. The divergence is cut off by a finite width of the sheet. The generic consequence is a series of collinear images. Each projected fold of the wave results in two density caustics. Each density caustic leads to two geometric lensing images, for a total of 4 images for each wave inflection. The two geometric image in each caustic are separated by the characteristic width of the sheet, if this is smaller than the Fresnel scale, the two images become effectively indistinguishable.

A large number of sheets might intersect the line of sight to any pulsar. Only those sufficiently inclined would lead to caustic formation. Empirically, some pulsar scattering appears dominated by a single sheet, leading to the prominent inverted arclets Stinebring et al. (2001).

3.1 Archival data of B0834+06

Our analysis is based on the apex data selected from the secondary spectrum of pulsar B0834+06 in (Brisken et al. 2010), which was observed as part of a 300 MHz global VLBI project on 2005 November 12, with GBT (GB), Arecibo (AR), Lovell and Westerbork (WB) telescopes. The GB-AR and AR-WB baselines are close to orthogonal and of comparable lengths, resulting in relatively isotropic astrometric positions. Information from each identified apex includes delay τ, delay rate (differential frequency f_D), relative Right Ascension $\Delta\alpha$ and relative declination $\Delta\delta$. Data of each apex are collected from four dual circular polarization 8 MHz wide sub-bands spanning the frequency range 310.5–342.5 MHz. As described in Brisken et al. (2010), the inverse parabolic arclets were fitted to positions of their apexes, resulting in a catalogue of apexes in each sub-band, each with delay and differential frequency. As previously described, the positions of the apexes appear constant across sub-bands. In this work, we first combine the apexes across sub-bands, resulting in a single set of images. We focus on the southern group with negative differential frequency: this grouping appears as a likely candidate for a double lensing screen. However, two groups (with positive/negative differential frequency) appear distinct in both the VLBI angular positions and the secondary spectra. We divide the apex data with negative f_D into two groups: in one group, time delay ranges from

0.1 ms to 0.4 ms, which we call 0.4 ms group, and in the other group, time delay at about 1 ms, which we call 1 ms group. In summary, the 0.4 ms group contains 10 apexes in the first two sub-bands, and 14 apexes in the last two sub-bands; the 1 ms group, contains 5, 6, 5 and 4 apexes in the four sub-bands subsequently, with center frequency of each band $f_{\rm band} = 314.5, 322.5, 330.5$ and 338.5 MHz.

We select the equivalent apexes from four sub-bands. To match the same apexes in different sub-bands, we scale the differential frequency in different sub-bands to 322.5 MHz, by $f_D/f_{\rm band} \cdot 322.5$ MHz. A total of 9 apexes from the 0.4 ms group and 5 apexes from the 1 ms group, were mapped by adjacent positions. This results in an estimation for the mean referenced frequency $f = 322.5$ MHz and a standard deviation among four sub-bands, listed in Table 2. The f_D and τ are the mean values of the four sub-bands, while the mean values of $\Delta\alpha$ and $\Delta\delta$ are the weighted mean.

We estimate the error of time delay τ, differential frequency f_D, $\Delta\alpha$ and $\Delta\delta$ listed in Table 2 from their band-to-band variance:

$$\sigma^2_{\tau,{\rm f_D},\Delta\alpha,\Delta\delta} = \frac{1}{n(n-1)}\sum_{i=1}^{4}(x_i - \bar{x})^2, \tag{1}$$

and $n = 4$ for four sub-bands.

3.2 One lens model

3.2.1 Distance to the lens

In the absence of a lens model, the fringe rate, delay and angular position cannot be uniquely related. To interpret the data, we adopt the lensing model of (Pen & Levin 2014). In this model, the lensing is due to projected fold caustics of a thin sheet closely aligned to the line of sight.

We define the *effective distance* $D_{\rm e}$ as

$$D_{\rm e} \equiv \frac{2c\tau}{\theta^2}. \tag{2}$$

And the differential frequency is related to the rate of change of delay as $f_D = -f\frac{{\rm d}\tau}{{\rm d}t}$. The effective distance corresponds to the pulsar distance $D_{\rm p}$, if the screen is exactly halfway. In general, $D_{\rm e} = D_{\rm p}D_{\rm s}/(D_{\rm p} - D_{\rm s})$ for a screen at $D_{\rm s}$.

When estimating the angular offset of each apex, we subtract the expected noise bias: $\theta^2 = (\Delta\alpha\cos(\delta))^2 + (\Delta\delta)^2 - \sigma^2_{\Delta\alpha} - \sigma^2_{\Delta\delta}$. We plot the θ *vs* square root of τ in Figure 1. A least square fit to the distance results in $D_{\rm 1e} = 1023 \pm 27$ pc for the 0.4 ms group, which we call lens 1, and $D_{\rm 2e} = 1281 \pm 82$ pc for the 1 ms group, hereafter lens 2. The errors, and uncertainties on the error, precludes a definitive interpretation of the apparent difference in distance. At face value, this indicates that the lens 2 is closer to the pulsar, and we will use this as a basis for the model in this paper. The distances are slightly different from those derived in Brisken et al. (2010), which is partly due to a different subset of arclets analysed. We discuss consequences of alternate interpretations in Section 3.4. The pulsar distance was directly measured using VLBI parallax to be $D_{\rm p} = 625 \pm 59$ pc. We take $D_{\rm 1e} = 1023$ pc, and the distance of lens 1 D_1, where 0.4 ms group scintillation points are refracted, as 388 pc. Similarly, for 1 ms apexes, the distance of lens 2 is taken as 420 pc, slightly closer to the pulsar.

For the 0.4 ms group, we adopt the geometry from

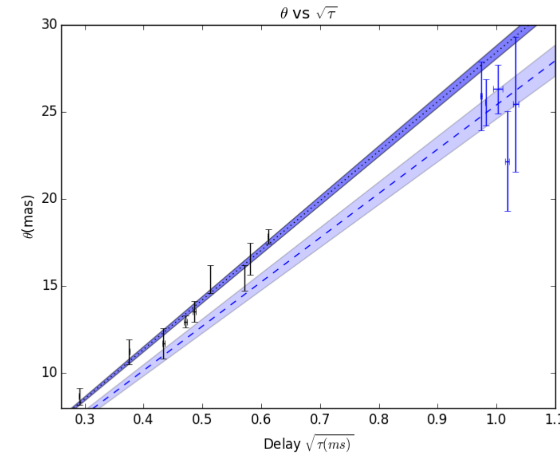

Figure 1. θ vs $\sqrt{\tau}$. Two separate lines through the origin were fitted to the points sampled among the 0.4 ms group and 1 ms group. The solid line is the fitted line of the 0.4 ms positions, where $D_{\rm 1e} = 1023$ pc with an error region of $\sigma_D = 27$ pc. The dashed lines are the fitted lines of the 1 ms position, where $D_{\rm 2e} = 1281$ pc with an error region $\sigma_D = 82$ pc.

Brisken et al. (2010), assigning these points along line AD as shown in Figure 2 based solely on their delay, which is the best measured observable. The line AD is taken as a fixed angle of $\gamma = -25^\circ.2$ east of the declination axis. We use this axis to define $\parallel$ and define $\perp$ by a 90° clockwise rotation.

3.2.2 Discussion of one lens model

The 0.4 ms group lens solution appears consistent with the premise of the inclined sheet lensing model (Pen & Levin 2014), which predicts collinear positions of lensing images. The time in last column of Table 2, which we denote as t_0, is calculated with $-2\tau f/f_D$, corresponds to the time required for the delay of an arclet to cross zero.

The collinearity can be considered a post-diction of this model. The precise positions of each image is random, and with 9 images no precision test is possible. The predictive power of sheet model becomes clear in the presence of a second, off-axis screen, which will be discussed below.

3.3 Double lens model

The apparent offset of the 1 ms group can be explained by a second lens screen. The small number of apexes at 1 ms suggests that the second lens screen involves a single caustic at a different distance. One expects each lens to re-image the full set of first scatterings, resulting in a number of apparent images equal to the product of number of lenses in each screen. In the primary lens system, the inclination appears such that typical waves form caustics. The number of sheets at shallower inclination increases as the square of the small angle. A 3 times less inclined sheet occurs 9 times as often. If a 1-σ wave forms a caustic in the primary lens, a 3 times less inclined surface only forms caustics for 3-σ waves, which occur two hundred times less often. Thus, one expects such sheets to only form isolated caustics, which we expect to see occasionally. Three free parameters describe a

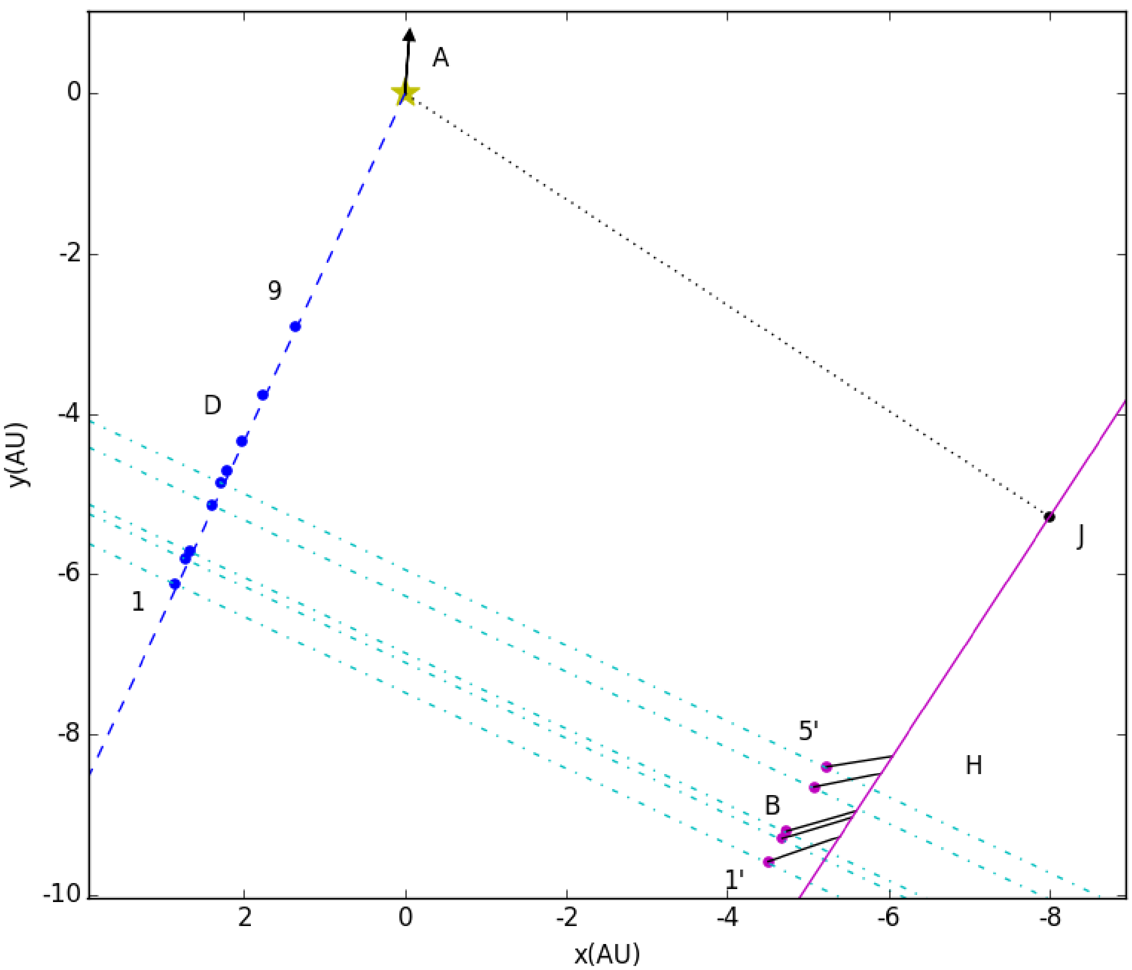

Figure 2. Angular positions of 0.4 ms and 1 ms group data in one lens model and double lens model. The axes represent the relative distance to the unrefracted pulsar in Right Ascension and declination directions, on a 2D plane that is transverse to the line of sight. On the left side, the group points marked with letter D, are the derived positions from the time delays of 0.4 ms group in one lens model. 388 pc away from the observer, the dashed line aligns the 0.4 ms apexes positions, with a angle $\gamma = -25^{\circ}.2$ east of north. The points on the right side, mark the first and second refraction images in double lens model. The unobservable points denoted as letter H, are the calculated positions on lens 2 from 1 ms group; the observable points denoted as letter B, are the calculated positions on lens 1 from 0.4 ms group. These two piles of refracted images are connected by the short solid lines. The long solid line is the inferred geometry of the second lens; while the dot dash lines, constructed perpendicular to the AD scattering axis, denote the positions of lens 1. The dotted line on the top right is perpendicular to the solid line, intersecting at J. The relative model pulsar-screen velocity is 187.9 km/s, with an angle $\epsilon = -4^{\circ}.34$ east of north, is marked with an arrow from the star, point A, at the top of the figure.

label	$\theta_{1\parallel}$(mas)	f_D(mHz)	τ(ms)	$\Delta\alpha$(mas)	$\Delta\delta$(mas)	t_0(days)
1	−17.39	−26.1(4)	0.3743(6)	8.5(3)	−15.7(3)	−107
2	−16.52	−24.9(4)	0.3378(3)	8.3(4)	−14.4(8)	−101
3	−16.24	−24.6(4)	0.327(3)	6.5(6)	−14.1(4)	−99.0
4	−14.59	−22.3(5)	0.2633(3)	6.2(3)	−14.2(7)	−88.1
5	−13.82	−21.2(6)	0.236(2)	5.1(4)	−12.6(5)	−83.3
6	−13.41	−20.4(5)	0.222(3)	5.6(3)	−11.73(8)	−81.4
7	−12.32	−18.9(2)	0.188(2)	5.1(6)	−10.6(6)	−74.2
8	−10.68	−16.8(3)	0.1412(9)	3.9(6)	−10.6(4)	−62.8
9	−8.26	−12.9(2)	0.0845(5)	2.9(3)	−8.2(4)	−48.7
1’	⋯	−43.1(4)	1.066(5)	−8(3)	−24(2)	−185
2’	⋯	−41.3(5)	1.037(3)	−11(1)	−19(3)	−188
3’	⋯	−40.2(6)	1.005(8)	−14(1)	−22.3(4)	−187
4’	⋯	−38.3(6)	0.9763(9)	−15(1)	−20.7(3)	−190
5’	⋯	−35.1(5)	0.950(2)	−15(1)	−21(1)	−202

Table 2. 0.4 ms and 1 ms reduced apex data. The upper part of the table list the 0.4 ms group data, while the 1 ms group lie in the lower part of the table. Observation data include the differential frequency f_D, time delay τ (τ_1 for 0.4 ms group and τ_2 for 1 ms group); $\Delta\alpha$ and $\Delta\delta$ are from the VLBI measurement. t_0 is the time at constant velocity for an apex to intersect the origin at constant speed along the main scattering parabola. More details in Section 3.1 and Section 3.2.2.

second caustic: distance, angle, and angular separation. We fix the distances from the effective VLBI distance (D_1 and D_2), and fit the angular separations and angles with the 5 delays of the 1 ms group.

3.3.1 Solving the double lens model

From Table 2, apexes 1’–5’ share a similar time delay, suggesting they are lensed by a common structure. We denote the position of the pulsar point A, positions of the lensed image on lens 2 point H, positions of the lensed image on lens 1 point B, position of the observer point O, AJ $\perp$ HJ at intersection point J, HF $\perp$ BD at intersection point F, BG $\perp$ HJ by intersection point G, for easier discussion.

The first step is to calculate the position of J. We make an estimate of the distance of J by the 1 ms θ–$\sqrt{\tau}$ relation (refer Figure 1). Then we calculated the position of J by matching the time delays of point 4’ and point 1’, which is then marked in Figure 2. The long solid line on the right side denotes the inferred geometry of lens 2, and by construction vertical to AJ.

The second step is to find the matched pairs of those two lenses. By inspection, we found that the 5 furthest points in 0.4 ms group match naturally to the double lens images. These five matched lines are marked with dot dash lines in Figure 2 and their values are listed in the second column in Table 4. They are the located at a distance 388 pc away from us. Here we define three distances:

$$\begin{aligned} D_{p2} &= 625 \text{ pc} - 420\text{pc} = 205 \text{ pc}, \\ D_{21} &= 420 \text{ pc} - 388 \text{ pc} = 32 \text{ pc}, \\ D_1 &= 388 \text{ pc} - 0 \text{ pc} = 388 \text{ pc}, \end{aligned} \tag{3}$$

where D_{p2} is the distance from the pulsar to lens 2, D_{21} is the distance from lens 2 to lens 1, and D_1 is the distance from lens 1 to the observer.

Figure 3 and Figure 4 are examples of how light are being refracted on the first lens plane and the second lens plane. We specifically choose the point with $\theta_{1\parallel}$ equal to −17.39 mas, which refer point 1’ on lens 2 as an example.

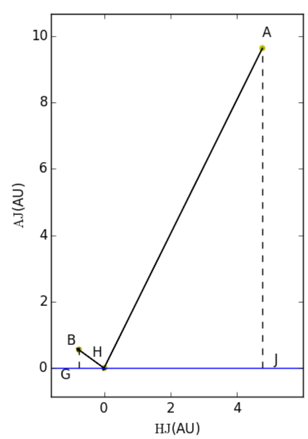

Figure 3. Refraction on lens 2. A is the position of the pulsar. H is the lensed image on lens 2. B is the lensed image on lens 1. AJ $\perp$ HJ and BG $\perp$ HJ. The values are illustrated for point 1’.

Considering the velocity of the photon parallel to the lens plane before and after refraction should be equal, we solve the solutions in double lens model using:

$$\begin{aligned} \frac{\text{JH}}{D_{p2}} &= \frac{\text{HG}}{D_{21}}, \\ \frac{\text{FB}}{D_{21}} &= \frac{\text{BD}}{D_1}. \end{aligned} \tag{4}$$

The solved positions are plotted in Figure 2, and respective time delays and differential frequencies are listed in Table 4. The error of time delay τ in double lens model is taken as

$$(\frac{\sigma_{\tau_i}}{\tau_{2i}})^2 = (\frac{\sigma_{\tau 1i}}{\tau_{1i}})^2 + (\frac{\sigma_{\tau 2i}}{\tau_{2i}})^2 + (\frac{\sigma_{\tau 2j}}{\tau_{2j}})^2, \tag{5}$$

where τ_1 and $\sigma_{\tau 1}$ represent the time delay and its error from the 0.4 ms group on lens 1, τ_2 and $\sigma_{\tau 2}$ represent the time delay and its error from respective 1 ms group on lens 2. And τ_{2j} is the τ_2 for the nearest point in reference in Table

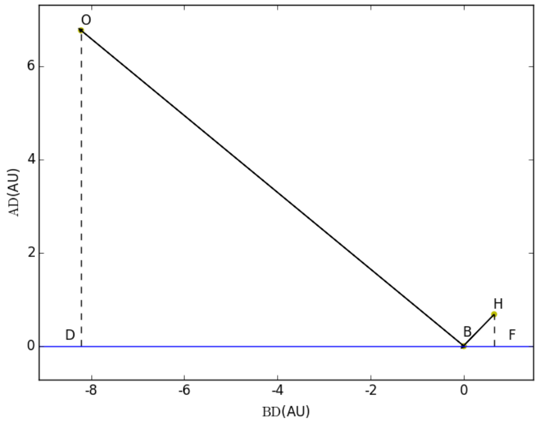

Figure 4. Refraction on lens 1. H is the lensed image on lens 2. B is the lensed image on lens 1. O is the position of the observer. HF $\perp$ DF and OD $\perp$ HJ. As in the previous figure, the values are illustrated for point 1'.

4 and $\sigma_{\tau 2j}$ is its error: for point $i = 5', 3'$, $j = 4'$; for point $i = 2'$, $j = 1'$.

For the error of differential frequency f_D, we add the error of the reference point (point 4') to the error of each other measured point:

$$(\frac{\sigma_{f_i}}{f_{Di}})^2 = (\frac{\sigma_{f_{Di}}}{f_{Di}})^2 + (\frac{\sigma_{f_{D4'}}}{f_{D4'}})^2 \qquad (6)$$

where $f_{D4'}$ and $\sigma_{f_{D4'}}$ are the differential frequency and its error of the point in the fourth row in Table 4.

3.3.2 *Comparing model results in double lens model with observations*

In order to compare τ, we calculate time delay τ_M for these five points, and list the results in Table 4. For points 4' and 1', they fit by construction since we use these to calculate the position of J; for the remaining three points, all of the results are within 3-σ of the observed time delays.

To compare differential frequency f_D, we need to calculate the velocity of the pulsar and the velocity of the lens. We take the lenses to be relative static, and solve for the velocity of the pulsar relative to the lens (in geocentric coordinate). The pulsar has two velocity components, and the two 1-D lenses effectively determine one component each. For $v_{\parallel}$, we derive the velocity 175.6 ± 2.7 km/s from f_D of point 1 in 0.4 ms group. The direct observable is the time to crossing of each caustic, denoted t_0 in Table 2.

To calculate $v_{\perp}$, we choose the point 4', which has the smallest errorbar of differential frequency. With $v_{\perp}$ to be 66.8 ± 2.8 km/s, we find $v_{\rm tot} = 187.9 \pm 2.8$ km/s, with an angle $\epsilon = 4^{\circ}.34$ west of north. This velocity represents the pulsar's relative velocity to the earth, subtracting the screen's relative velocity to the earth. The model derived and observation velocities (heliocentric and in Local Standard of Rest) are listed in Table 3. The direction of the model velocity is marked on the top of the star in Figure 2.

With this velocity of the pulsar, we calculate the differential frequency f_M of points 5',3',2' and 1'. Results are listed in Table 4. The calculated results all lie within the 3-σ error intervals of the observed data.

The reduced χ^2 for time delay τ is 1.5 for 3 degrees of freedom and 2.1 for f_D for 4 degrees of freedom. This is consistent with the model.

Within this lensing model, we can test if the caustics are parallel. Using the lag error range of double lensed point 4 (the best constrained), we find a 1-σ allowed angle of 0.4 degrees from parallel with the whole lensing system. This lends support of a highly inclined sheet, probably aligned to better than 1%.

3.3.3 *Discussion of double lens model*

For 1 ms group, lens 2 only images a subset of the lens 1 images. This could happen if lens 1 screen is just under the critical inclination angle, such that only 3-σ waves lead to a fold caustic. If the lens 2 was at a critical angle, the chance of encountering a somewhat less inclined system is of order unity. More surprising is the absence of a single refraction image of the pulsar, which is expected at position J. This could happen if the maximum refraction angle is just below critical, such that only rays on the appropriately aligned double refraction can form images. We plot the refraction angle β in the direction that is transverse to the first lens plane in Figure 5. The data spans about 10% in frequency, making it unlikely that single lens image J would not be seen due to the larger required refraction angle. Instead, we speculate that the fold caustic could have formed near double lens image 1, and thus only intersections with the closer lens plane caustic south of image 1 are double lensed.

This is a generic outcome of a swallowtail catastrophe (Arnold 1990). In this picture, the sheet just starts folding near point 5'. North of point 5', no fold appears in projection. Far south of point 5', a full fold exhibits two caustics emanating from the fold cusp. Near the cusp the magnification is the superposition of two caustics, leading to enhanced lensing and higher likelihood of being observed.

We denote t_1 the time that the lensed image on lens 2 to move from point H to point J. From our calculation, 57 days earlier the single lensed pulsar image J would have appeared overlayed on point 5'; and 77 days before Nov 12, 2005, it overlayed on point 1'. The model predicts the presence of a single lensed image refracted at these points, in addition to the double lensed images.

3.4 Distance Degeneracies

With two lens screens, the number of observables increases: in principle one could observe both single reflection delays and angular positions, as well as the double reflection delay and angular position. Three distances are unknown, equal to the number of observables. Unfortunately, these measurements are degenerate, which can be seen as follows. From the two screens $i = 1, 2$, the two single deflection effective distance observables are $D_{i\rm e} \equiv 2c\tau_i/\theta_i^2 = D_i^2(1/D_i + 1/D_{pi})$. A third observable effective distance is that of screen 2 using screen 1 as a lens, $D_{21\rm e} = D_1^2(1/D_1 + 1/D_{21})$, within the triangle that is formed by lens 1, lens 2 and the observer. That is also algebraically derivable from the first two relations: $D_{21\rm e} = D_{1\rm e}D_{2\rm e}/(D_{2\rm e} - D_{1\rm e})$.

Parameter	$\mu_{\alpha*}$(mas/year)	μ_δ(mas/year)	μ_{l*}(mas/year)	μ_b (mas/year)
model pulsar-screen velocity	-6.11 ± 0.95	62.43 ± 0.95	-57.21	21.68
VLBI pulsar proper motion	2.14 ± 0.21	51.64 ± 0.13	-46.68	27.98
Screen motion	$\cdots$	$\cdots$	10.53	6.29

Table 3. Summary of velocities in double lens model. The velocities listed in equatorial coodinates are the relative velocity in heliocentric system, while the velocities in galactic coordinates are the relative velocities in LSR (Local Standard of Rest). The screen is only moving slowly ($\sim$ 30km/s).

label	$\theta_{1\parallel}$ (mas)	τ_2(ms)	σ_τ(ms)	τ_M(ms)	f_D(mHz)	σ_f(mHz)	f_M(mHz)	t_1(days)
1'	-17.39	1.0663	0.0050	1.0663*	-43.08	0.83	-42.27	-77
2'	-16.52	1.0370	0.0059	1.0362	-41.27	0.87	-41.04	-72
3'	-16.24	1.005	0.011	1.027	-40.17	0.87	-40.65	-70
4'	-14.59	0.9763	0.00088	0.9763*	-38.31	0.64	$-38.31\dagger$	-62
5'	-13.82	0.9495	0.0094	0.9551	-35.06	0.81	-37.23	-57

Table 4. Comparison of time delay τ and the differential frequency f_D of the observation and the model fitting result in the double lens model. $\theta_{1\parallel}$ denotes the angular offsets of the corresponding images at lens 1. The values with star symbols on them are the points that we use to calculate the position of J and the point with a $\dagger$ symbol is the point that we use to calculate the transverse velocity of the pulsar $v_\perp$. They agree with data by construction.

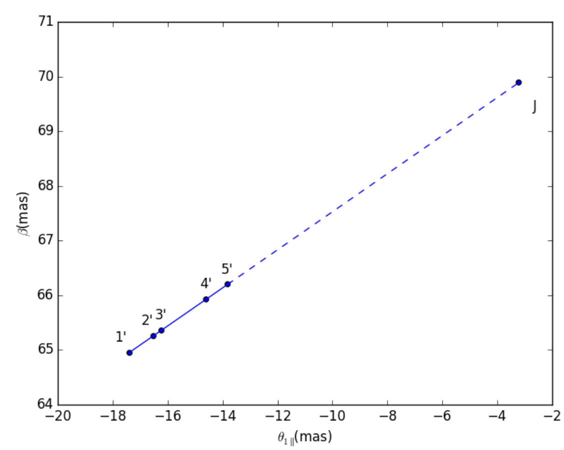

Figure 5. Deflection angle $\beta = \pi - \angle$AHB on lens 2. Point J denotes the expected position to form a single refraction image, which was not observed. The small change in angle relative to the observed images precludes a finite refraction cut-off, since the data spans 10% bandwidth, with a 20% change in refractive strength. We propose a swallowtail caustic as the likely origin for the termination of the second lens sheet.

In this archival data set, the direct single lens from the further plane at position J is missing. It would have been visible 57 days earlier. The difference in time delays to image J and the double reflection images would allow a direct determination of the effective distance to lens plane 2. Due to the close to 90 degree angle $\angle$DAJ between lenses, the effect would be about a factor of 10 ill conditioned. With sufficiently precise VLBI imaging one could distinguish if the double refracted images are at position B (if lens 1 is closer to the observer) or position H (if lens 2 is closer to the observer). As described above, we interpret the effective distances to place screen 2 further away.

4 DISCUSSIONS

4.1 Interpretation

The relative motion between pulsar and lens is directly measured by the differential frequency, and not sensitive to details of this model. Brisken et al. (2010) derived similar motions. This motion is in broad agreement with direct VLBI proper motion measurement, requiring the lens to be moving slowly compared to the pulsar proper motion or the LSR. The lens is $\sim$ 200 pc above the galactic disk. Matter can either be in pressure equilibrium, or in free-fall, or some combination thereof. In free fall, one expects substantial motions. These data rule out retrograde or radially galactic orbits: the lens is co-rotating with the galaxy. In pressure equilibrium, gas rotates slower as its pressure scale height increases, which appears consistent with the observed slightly slower than co-rotating motion. The modest lens velocities also appear consistent with the general motion of the ISM, perhaps driven by galactic fountains (Shapiro & Field 1976) at these latitudes above the disk. In the inclined sheet model, the waves move at Alfvénic speed, but due to the high inclination, will move sub percent of this speed in projection on the sky, and completely negligible compared to other sources of motion.

Alternative models, for example, evaporating clouds (Walker & Wardle 1998) or strange matter (Pérez-García et al. 2013), do not make clear predictions. One would expect higher proper motions from these freely orbiting sources, larger future scintillation samples may constrain these models.

In order to incline one sheet randomly to better than 1% requires of order 10^4 randomly placed sheets, i.e. many per parsec. This sheet extends for $\sim$ 10 AU in projection, corresponding to a physical scale greater than 1000 AU. These two numbers roughly agree, leading to a physical picture of magnetic domain boundaries every $\sim$ 0.1 pc. B0834+06 has had noted arcs for multiple years, perhaps suggesting this dominant lens plane is larger than typical. One might expect to reach the end of the sheet within decades.

A generic prediction of the inclined sheets is a change in rotation measure across the scattering length. Over 1000 AU, one might expect a typical RM (rotation measure) change of 10^{-3} rad/m^2. At low frequencies, for example in LOFAR[1] or GMRT[2], the size of the scattering screen extends another order of magnitude in angular size, and RM changes increase to ~ 0.01, which is plausibly measurable.

4.2 Possible Improvements

We discuss several strategies which can improve on the solution accuracy. The single biggest improvement would be to monitor over several months, as the pulsar crosses each individual lens, including both lensing systems. This allows a direct comparison of single lens to double lens arclets.

Angular resolution can be improved using longer baselines, for example adding a GMRT-GBT baseline doubles the resolution. Observing at multiple frequencies over a longer period allows for a more precise measurement: when the pulsar is between two lenses, the refraction angle β is small, and one expects to see the lensing at higher frequency, where the resolution is higher, and distances between lens positions can be measured to much higher accuracy.

Holographic techniques (Walker et al. 2008; Pen et al. 2014) may be able to measure delays, fringe rates, and VLBI positions substantially more accurately. Combining these techniques, the interstellar lensing could conceivably achieve distance measurements an order of magnitude better than the current published effective distance errors. This could bring most pulsar timing array targets into the coherent timing regime, enabling arc minute localization of gravitational wave sources, lifting any potential source confusion.

Ultimately, the precision of the lensing results would be limited by the fidelity of the lensing model. In the inclined sheet model, the images move along fold caustics. The straightness of these caustics depends on the inclination angle, which in turn depends on the amplitude of the surface waves.

5 CONCLUSIONS

We have applied the (Pen & Levin 2014) inclined sheet model to archival apex data of PSR B0834+06. The data is well fit by two linear lensing screens, with nearly plane-parallel geometry. The second screen provides a precision test with 10 observables (5 time delays and 5 differential frequencies) and 3 free parameters. The model fits the data to non-trivial percent accuracy on each of 7 data points. This natural consequence of very smooth reconnection sheets is an unlikely outcome of ISM turbulence. These results, if extrapolated to multi-epoch observations of binary systems, might result in accurate distance determinations and opportunities for removing scattering induced timing errors. This approach also opens the window to measuring precise transverse motions of the ionized ISM outside the galactic plane.

[1] http://www.lofar.org/
[2] http://gmrt.ncra.tifr.res.in/

6 ACKNOWLEDGEMENTS

We thank NSERC for support. We acknowledge helpful discussions with Peter Goldreich and M. van Kerkwijk. Siqi Liu thank the useful discussion with Robert Main and JD Emberson on improving the expression of the content. The National Radio Astronomy Observatory is a facility of the National Science Foundation operated under cooperative agreement by Associated Universities, Inc.

REFERENCES

Arnold V. I., 1990, Singularities of Caustics and Wave Fronts. Springer Netherlands
Boyle L., Pen U.-L., 2012, Phys. Rev. D, 86, 124028
Braithwaite J., 2015, MNRAS, 450, 3201
Brisken W. F., Macquart J.-P., Gao J. J., Rickett B. J., Coles W. A., Deller A. T., Tingay S. J., West C. J., 2010, ApJ, 708, 232
Clegg A. W., Fey A. L., Lazio T. J. W., 1998, ApJ, 496, 253
Deller A. T., Archibald A. M., Brisken W. F., Chatterjee S., Janssen G. H., Kaspi V. M., Lorimer D., Lyne A. G., McLaughlin M. A., Ransom S., Stairs I. H., Stappers B., 2012, ApJ, 756, L25
Deller A. T., Boyles J., Lorimer D. R., Kaspi V. M., McLaughlin M. A., Ransom S., Stairs I. H., Stovall K., 2013, ApJ, 770, 145
Efron B., Tibshirani R., 1991, Science, 253, 390
Kramer M., Stairs I. H., Manchester R. N., McLaughlin M. A., Lyne A. G., Ferdman R. D., Burgay M., Lorimer D. R., Possenti A., D'Amico N., Sarkissian J. M., Hobbs G. B., Reynolds J. E., Freire P. C. C., Camilo F., 2006, Science, 314, 97
Longuet-Higgins M. S., 1960, J. Opt. Soc. Am., 50, 845
Lorimer D. R., Kramer M., 2012, Handbook of Pulsar Astronomy
Pen U.-L., King L., 2012, MNRAS, 421, L132
Pen U.-L., Levin Y., 2014, MNRAS, 442, 3338
Pen U.-L., Macquart J.-P., Deller A. T., Brisken W., 2014, MNRAS, 440, L36
Pérez-García M. Á., Silk J., Pen U.-L., 2013, Physics Letters B, 727, 357
Shapiro P. R., Field G. B., 1976, ApJ, 205, 762
Stinebring D. R., McLaughlin M. A., Cordes J. M., Becker K. M., Goodman J. E. E., Kramer M. A., Sheckard J. L., Smith C. T., 2001, ApJ, 549, L97
Walker M., Wardle M., 1998, ApJ, 498, L125
Walker M. A., Koopmans L. V. E., Stinebring D. R., van Straten W., 2008, MNRAS, 388, 1214